Comput Mech (2010) 46:53–67
DOI 10.1007/s00466-010-0486-0

ORIGINAL PAPER

3D fluid–structure-contact interaction based on a combined XFEM FSI and dual mortar contact approach

Ursula M. Mayer · Alexander Popp · Axel Gerstenberger · Wolfgang A. Wall

Received: 3 November 2009 / Accepted: 17 February 2010 / Published online: 23 March 2010

Abstract Finite deformation contact of flexible solids embedded in fluid flows occurs in a wide range of engineering scenarios. We propose a novel three-dimensional finite element approach in order to tackle this problem class. The proposed method consists of a dual mortar contact formulation, which is algorithmically integrated into an eXtended finite element method (XFEM) fluid–structure interaction approach. The combined XFEM fluid–structure-contact interaction method (FSCI) allows to compute contact of arbitrarily moving and deforming structures embedded in an arbitrary flow field. In this paper, the fluid is described by instationary incompressible Navier–Stokes equations. An exact fluid–structure interface representation permits to capture flow patterns around contacting structures very accurately as well as to simulate dry contact between structures. No restrictions arise for the structural and the contact formulation. We derive a linearized monolithic system of equations, which contains the fluid formulation, the structural formulation, the contact formulation as well as the coupling conditions at the fluid–structure interface. The linearized system may be solved either by partitioned or by monolithic fluid–structure coupling algorithms. Two numerical examples are presented to illustrate the capability of the proposed fluid–structure-contact interaction approach.

Keywords Finite deformation contact · Contact of solids in fluid · EXtended finite element method · Fluid–structure interaction · Dual mortar contact approach · Partitioned and monolithic fluid–structure coupling

U. M. Mayer · A. Popp · A. Gerstenberger · W. A. Wall (✉)
Institute for Computational Mechanics, Technische Universität München, Boltzmannstrasse 15, 85747 Garching, Germany
e-mail: wall@lnm.mw.tum.de

1 Introduction

A variety of problems in engineering and applied sciences require the simulation of finite deformation contact interactions of solids surrounded by fluid. Important fields of application include machine parts, such as gaskets or sliding-contact bearings, and biomechanical systems, such as heart valves or capillary flow of red blood cells, to name only a few.

From the method development point of view, fluid–structure interaction (FSI) problems coupled with structural contact require powerful simulation approaches for both algorithmic 'building blocks': FSI and contact. Even though many different FSI approaches and contact formulations exist, most of them are hard or even impossible to combine algorithmically with a reasonable programming effort. Arbitrary Lagrangian–Eulerian (ALE) methods are a very popular category of FSI methods. For this type of FSI approaches, the fluid mesh is connected to the solid mesh and deforms according to the structural deformations. Problems occur in the case of contact, since fluid elements between contact interfaces are completely squeezed together. This feature complicates the application of ALE methods for simulations of dry contact. Fictitious Domain (FD) methods and Immersed Boundary Methods (IMB) usually lack an exact fluid–structure interface representation within a fixed background grid. Dry contact is hard to be achieved under such restrictions.

A contact formulation is needed as second 'building block' for the proposed FSCI approach. Contact ought to be treated efficiently and as general as possible, allowing for very large structural deformations of the contacting elastic bodies. For this purpose, both a suitable contact discretization and a suitable scheme for constraint enforcement have to be chosen. Concerning discretization, several authors (see e.g. [12,14,24,25,39]) have demonstrated over the last decade

the superior robustness of mortar-based segment-to-segment methods as compared with classical node-to-segment schemes. Constraint enforcement is usually handled via Lagrange multipliers or a penalty method.

First efforts in developing numerical approaches for FSI including contact so far concentrate on tailored, often simplified models for very specific problem scenarios. In [31], a 2D fluid–structure interaction (FSI) method with a purely node-based contact algorithm within a monolithic solution scheme is proposed for the numerical simulation of heart valve dynamics. Another approach dealing with the dynamics of thin valves in fluid is presented in [4], where a partitioned FD based FSI scheme is combined with a specific contact formulation for thin structures (modeled as 1D continua) and rigid walls. An interesting extension to fully 3D aortic valve simulations including elastic contact has been proposed recently [1]. Modeling of FSI problems including contact is also considered in [27] and [30], where the authors introduce a so-called surface-edge-node contact tracking algorithm used in combination with the Deforming-Spatial-Domain/Stabilized Space–Time (DSD/SST) formulation [28,29]. When two bodies approach each other, penalty forces are applied in such a way that the contacting surfaces are kept slightly apart in order to protect the fluid mesh in between. Furthermore, current research focuses on the detailed analysis of physical effects in the contact interface such as lubrication or wet contact (see e.g. [38]). In this case, the space between contacting solids is partially filled with fluid, which constitutes a specific class of problems (based on the Reynolds equation for the thin fluid film and a free boundary).

The main scope of our paper is to bring together recent developments in the fields of fluid–structure interaction and computational contact mechanics in order to create a novel and very general numerical approach: we propose a 3D finite element formulation, which combines an eXtended finite element method (XFEM) FSI method and a dual finite deformation mortar contact formulation. Owing to its generality, the resulting FSI-contact (FSCI) method is applicable to a broad range of problems involving elastic contact of solids embedded in an interacting flow field. We start the derivation of our FSCI method by reviewing a two-field XFEM FSI method [7–10] and related other methods [32,34]. The fluid fields and the structural fields live on two distinct grids. An interface handling algorithm (see [17] and [19]) allows to localize the fluid–structure interface of arbitrarily moving as well as deforming structures and provides an exact representation of the discretized interface within the fixed fluid background mesh. Continuity between nonmatching fluid and interface grids is weakly imposed by a stress based Lagrange multiplier technique [9] that is numerically stable without heuristic stabilization parameters and does not generate a saddle point structure for the resulting FSI system. These features are mainly responsible for the convenient integration of the contact formulation. In addition, they prevent that any limitations to the structural as well as to the contact formulation occur. Flow patterns around surfaces very close to contact can be resolved highly accurately. An exactly represented interface also allows to simulate dry contact, since no fluid computation is performed between structures in contact. Regarding the contact formulation, we employ a recently developed mortar approach [11,21,22] based on so-called dual Lagrange multipliers in combination with a primal-dual active set strategy for contact constraint enforcement. By interpreting the active set search as semi-smooth Newton scheme and by performing consistent linearization, all types of nonlinearities (i.e. geometrical, material and contact) are efficiently resolved within one single iterative scheme. The dual Lagrange multipliers (see e.g. [36]) can be eliminated by condensation, thus avoiding an undesirable increase in global system size. The final structural system of equations including contact is positive definite and contains only displacement degrees of freedom. All described properties heavily facilitate the proposed integration into our FSI approach. A linearized coupled system of equations is derived, which contains the fluid description, the structural description, the contact formulation as well as the FSI coupling conditions. Any partitioned or monolithic fluid–structure coupling algorithm may be applied to solve the system of equations.

The remainder of the paper is organized as follows: the general problem setup is described in Sect. 2. We proceed with a review of the XFEM fluid–structure interaction approach in Sect. 3, where we focus on details regarding the combination with the contact method. The important aspects of the dual mortar contact formulation are explained in Sect. 4. The linearized FSCI system, which may be solved by partitioned or monolithic fluid–structure coupling schemes, is derived in Sect. 5. Numerical examples demonstrate the capability of the approach in Sect. 6.

2 General formulation of the fluid–structure-contact interaction problem

To begin with, we introduce the general problem statement. Figure 1 displays the coupled system and introduces the fluid fields for velocity $\boldsymbol{u}$ and pressure p in the fluid domain Ω^f as well as the structural displacement field $\boldsymbol{d}^s$ in the structural domain Ω^s. Fluid quantities are denoted by a superscript f if necessary for understanding; structural quantities are always denoted by a superscript s if the entire structure is addressed. To prepare the integration of a contact formulation, the structural domain Ω^s already consists of two contacting bodies distinguished by superscripts s, (1) and s, (2). The fluid–structure interface is denoted by Γ_{FSI}.

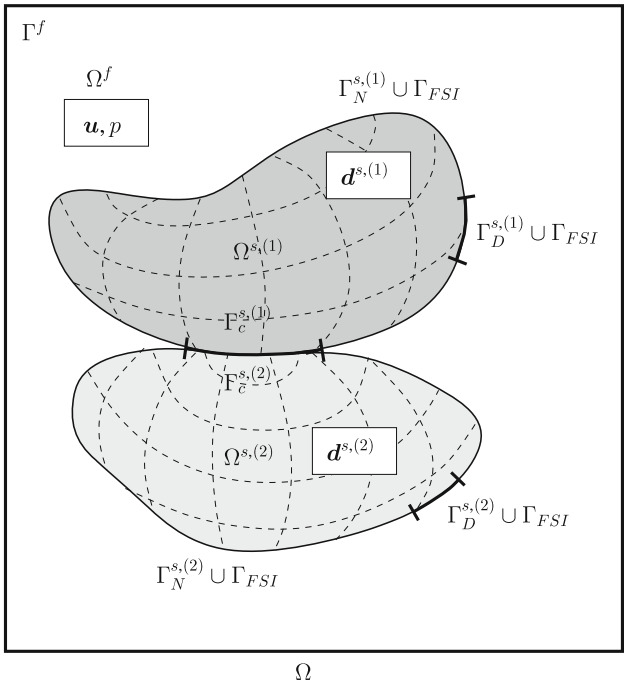

Fig. 1 Coupled system comprising fluid and structural fields

2.1 Fluid

The presented approach is not limited to a specific flow description. For the derivation and our numerical examples we describe the fluid part by instationary, incompressible Navier–Stokes equations for Newtonian fluids. The stress tensor $\boldsymbol{\sigma}^f$ for Newtonian fluids

$$\boldsymbol{\sigma}^f = -p\boldsymbol{I} + 2\mu\boldsymbol{\epsilon}(\boldsymbol{u}) \tag{1}$$

is composed of a hydrostatic term $p\boldsymbol{I}$ and a viscous term $2\mu\boldsymbol{\epsilon}(\boldsymbol{u})$, where μ denotes the dynamic viscosity. The strain rate tensor $\boldsymbol{\epsilon}(\boldsymbol{u})$ may be written as

$$\boldsymbol{\epsilon}(\boldsymbol{u}) = \frac{1}{2}\left(\nabla\boldsymbol{u} + (\nabla\boldsymbol{u})^T\right). \tag{2}$$

The conservation of momentum in Eulerian formulation is

$$\rho\frac{\partial\boldsymbol{u}}{\partial t} = -\rho\boldsymbol{u}\cdot\nabla\boldsymbol{u} + \nabla\cdot\boldsymbol{\sigma}^f + \boldsymbol{b}^f \quad \text{in } \Omega^f. \tag{3}$$

The body force $\boldsymbol{b}^f$ is omitted in further derivations, but it may be included without additional difficulties and it is also integrated in the implementation.

Mass conservation for an incompressible flow field requires the divergence of the velocity $\boldsymbol{u}$ to equal zero

$$\nabla\cdot\boldsymbol{u} = 0. \tag{4}$$

Dirichlet and Neumann boundary conditions Γ_D^f and Γ_N^f at the fluid boundary may be stated as

$$\boldsymbol{u} = \bar{\boldsymbol{u}} \quad \text{in } \Gamma_D^f, \tag{5}$$

$$\boldsymbol{n}^f\cdot\boldsymbol{\sigma}^f = \bar{\boldsymbol{h}}^f \quad \text{in } \Gamma_N^f. \tag{6}$$

The weak form is obtained by testing Eqs. (3) and (4) with test functions for velocity $\boldsymbol{v}$ and pressure q

$$\left(\boldsymbol{v}, \rho\frac{\partial\boldsymbol{u}}{\partial t}\right)_{\Omega^f} + (\boldsymbol{v}, \rho\boldsymbol{u}\cdot\nabla\boldsymbol{u})_{\Omega^f} + \left(\nabla\boldsymbol{v}, \boldsymbol{\sigma}^f\right)_{\Omega^f} + (q, \nabla\cdot\boldsymbol{u})_{\Omega^f} - \left(\boldsymbol{v}, \bar{\boldsymbol{h}}^f\right)_{\Gamma_N^f} = 0. \tag{7}$$

During the development of the XFEM FSI approach in Sect. 3, we reformulate the weak form to include a moving interface based on embedded Dirichlet conditions.

2.2 Structure

Before considering contact interactions and FSI of two bodies, the continuum mechanics problem statement of one single structure is briefly reviewed. As usual for most applications, the structural behavior is described based on a Lagrangian description, where the motion from reference configuration $\boldsymbol{x}_0^s$ to current configuration $\boldsymbol{x}^s$ is given by the displacement vector $\boldsymbol{d}^s = \boldsymbol{x}^s - \boldsymbol{x}_0^s$. The structural velocity $\dot{\boldsymbol{d}}^s$ and the structural acceleration $\ddot{\boldsymbol{d}}^s$ are defined as

$$\ddot{\boldsymbol{d}}^s = \frac{\partial\dot{\boldsymbol{d}}^s}{\partial t} = \frac{\partial^2\boldsymbol{d}^s}{\partial t^2}. \tag{8}$$

As can be seen in Fig. 1, the structural domain is represented by the open set Ω^s in the current configuration and the boundary $\partial\Omega^s$ consists of Dirichlet boundary Γ_D^s and Neumann boundary Γ_N^s. For convenience and without loss of generality, material nonlinearity is simply incorporated by assuming compressible Neo-Hookean behavior

$$\mathbf{S} = \frac{\partial\Psi_{NH}}{\partial\mathbf{E}}, \quad \mathbb{C} = \frac{\partial^2\Psi_{NH}}{\partial\mathbf{E}^2}, \tag{9}$$

where the second Piola–Kirchhoff stress tensor $\boldsymbol{S}$, the hyperelastic strain energy function Ψ_{NH}, the fourth order constitutive tensor $\mathbb{C}$ and the Green–Lagrange strain tensor $\mathbf{E}$ are introduced. The strain tensor can be written in terms of the material deformation gradient $\mathbf{F}$ as $\mathbf{E} = \frac{1}{2}(\mathbf{F}^T\mathbf{F} - \boldsymbol{I})$, and the second Piola–Kirchhoff stress tensor $\boldsymbol{S}$ is obtained from the Cauchy stress $\boldsymbol{\sigma}$ as $\boldsymbol{S} = J\boldsymbol{F}^{-1}\cdot\boldsymbol{\sigma}\cdot\boldsymbol{F}^{-T}$. Here J denotes the determinant of the material deformation gradient $\boldsymbol{F}$, which itself is defined as

$$\boldsymbol{F} = \frac{\partial\boldsymbol{x}^s}{\partial\boldsymbol{x}_0^s}. \tag{10}$$

The initial boundary value problem (IBVP) of finite deformation elastodynamics stated in the current configuration is

$$\begin{aligned} \nabla \cdot \boldsymbol{\sigma}^s + \boldsymbol{b}^s &= \rho^s \ddot{\boldsymbol{d}}^s \quad \text{in } \Omega^s, \\ \boldsymbol{d}^s &= \bar{\boldsymbol{d}}^s \quad \text{on } \Gamma_D^s, \\ \boldsymbol{\sigma}^s \cdot \boldsymbol{n}^s &= \bar{\boldsymbol{h}}^s \quad \text{on } \Gamma_N^s, \end{aligned} \tag{11}$$

where ρ^s is the current structural density. Prescribed displacements are represented by $\bar{\boldsymbol{d}}^s$ and prescribed surface tractions by $\bar{\boldsymbol{h}}^s$, whereas $\boldsymbol{b}^s$ denotes a volumetric body force. Initial conditions for structural displacements and structural velocities can be formulated as $\boldsymbol{d}^s(\boldsymbol{x}, t = 0) = \boldsymbol{d}_0^s$ and $\dot{\boldsymbol{d}}^s(\boldsymbol{x}, t = 0) = \dot{\boldsymbol{d}}_0^s$. The weak form after integration by parts (still without consideration of the fluid–structure coupling and without consideration of contact) is

$$\begin{aligned} &(\delta \boldsymbol{d}^s, \rho^s \ddot{\boldsymbol{d}}^s)_{\Omega^s} + (\nabla \delta \boldsymbol{d}^s, \boldsymbol{\sigma}^s)_{\Omega^s} - (\delta \boldsymbol{d}^s, \boldsymbol{b}^s)_{\Omega^s} \\ &\quad - (\delta \boldsymbol{d}^s, \bar{\boldsymbol{h}}^s)_{\Gamma_N^s} = 0. \end{aligned} \tag{12}$$

This equation is discretized using any standard (often mixed/hybrid) finite element technique in space and direct time integration schemes. Geometrical and material nonlinearities are handled via a Newton–Raphson method. A brief overview of spatial discretization and time integration will be given in Sect. 3.5.

2.3 Contact

We restrict the presentation to only two contacting structures as depicted in Fig. 2, yet a generalization to an arbitrary number of bodies is straightforward and mostly a matter of efficient contact search strategies. The structural domain Ω^s in the current configuration consists of two separate open sets $\Omega^{s,(1)}$ and $\Omega^{s,(2)}$, see also Fig. 1. As the two bodies may potentially come into contact, their surfaces $\partial\Omega^{s,(i)}, i = 1, 2$, are divided into three boundary sets as

$$\begin{aligned} \partial\Omega^{s,(i)} &= \Gamma_D^{s,(i)} \cup \Gamma_N^{s,(i)} \cup \Gamma_c^{s,(i)}, \\ \Gamma_D^{s,(i)} \cap \Gamma_N^{s,(i)} &= \Gamma_D^{s,(i)} \cap \Gamma_c^{s,(i)} = \emptyset, \end{aligned} \tag{13}$$

where $\Gamma_c^{s,(i)}$ now represents the potential contact surface in addition to the well-known Dirichlet and Neumann boundaries. Note that FSI is still not considered. We retain a common nomenclature in contact mechanics here and refer to $\Gamma_c^{s,(1)}$ as the slave surface and to $\Gamma_c^{s,(2)}$ as the master surface, although their traditional meaning will not be conveyed to our mortar discretization approach. All definitions given in Sect. 2.2 for one single structure, such as stress and strain tensors, the IBVP and weak form, hold for two bodies in full analogy.

Proximity and potential contact of the two bodies is measured by the gap function $g(\boldsymbol{x})$ in the current configuration

$$g(\boldsymbol{x}) = -\boldsymbol{n}^c \left(\boldsymbol{x}^{s,(1)}\right) \cdot \left[\boldsymbol{x}^{s,(1)} - \hat{\boldsymbol{x}}^{s,(2)}\right], \tag{14}$$

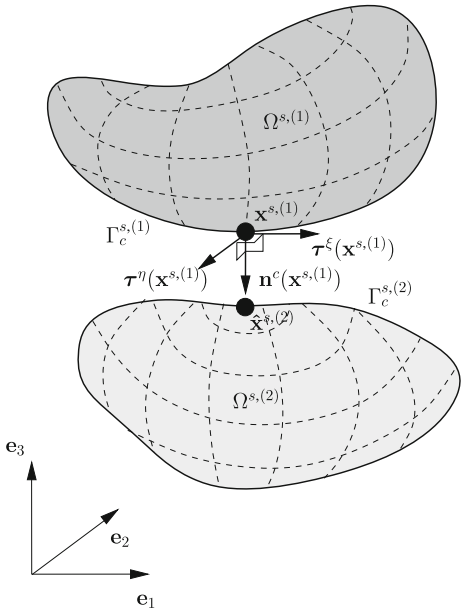

Fig. 2 Setup of the 3D finite deformation contact problem

where $\boldsymbol{n}^c$ represents the current outward unit normal on the slave surface $\Gamma_c^{s,(1)}$ in $\boldsymbol{x}^{s,(1)}$ and $\hat{\boldsymbol{x}}^{s,(2)}$ denotes the projection of $\boldsymbol{x}^{s,(1)}$ onto the master surface $\Gamma_c^{s,(2)}$ along $\boldsymbol{n}^c$, see Fig. 2. The definition of the contact normal $\boldsymbol{n}^c$ within our finite element discretization will be discussed briefly in Sect. 4.3. Together with the two tangent vectors $\boldsymbol{\tau}^{\xi}$ and $\boldsymbol{\tau}^{\eta}$, $\boldsymbol{n}^c$ builds an orthonormal basis in the slave surface point $\boldsymbol{x}^{s,(1)}$.

A Lagrange multiplier vector $\boldsymbol{\lambda}$ is defined as negative contact traction on the slave surface ($\boldsymbol{\lambda} = -\boldsymbol{h}_c^{s,(1)}$), providing the basis for a mixed variational formulation later to be discretized with a dual mortar finite element approach [21,22]. We denote the normal and tangential components of the Lagrange multiplier vector $\boldsymbol{\lambda}$ as $\lambda_n \boldsymbol{n}^c$, $\lambda_\tau^{\xi} \boldsymbol{\tau}^{\xi}$ and $\lambda_\tau^{\eta} \boldsymbol{\tau}^{\eta}$ respectively.

Two modifications of the structure problem statement have to be taken into account when considering contact: an additional *contact virtual work* term entering the weak form (12) and a set of *contact constraints*. First, contact virtual work is readily expressed in terms of a slave side integral by exploiting the balance of linear momentum across the contact interface, yielding

$$\delta \Pi_c = \left(\boldsymbol{\lambda}, \delta \boldsymbol{d}^{s,(1)} - \delta \boldsymbol{d}^{s,(2)}\right)_{\Gamma_c^{s,(1)}}. \tag{15}$$

Contact constraints are addressed next. Frictionless contact interaction is governed by the three classical Karush–Kuhn–Tucker (KKT) conditions and frictionless tangential sliding

$$g(\boldsymbol{x}) \geq 0, \quad \lambda_n \geq 0, \quad \lambda_n \, g(\boldsymbol{x}) = 0, \quad \lambda_\tau^{\xi} = \lambda_\tau^{\eta} = 0. \tag{16}$$

The interested reader is referred to [16,37] for details on constitutive laws for contact including friction. Note that the strong pointwise non-penetration condition $g(\boldsymbol{x}) \geq 0$

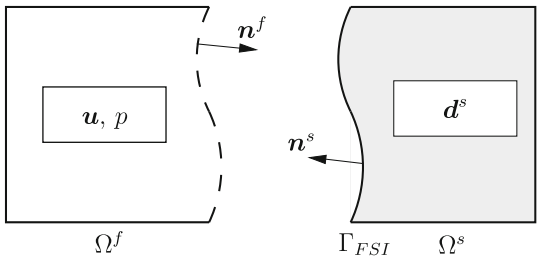

Fig. 3 Definition of normals in the coupled problem

is typically replaced by a weak integral condition along the contact interface in the context of a mortar approach

$$(\delta\lambda_n, g(\boldsymbol{x}))_{\Gamma_c^{s,(1)}} \geq 0, \tag{17}$$

where Lagrange multiplier test functions $\delta\lambda_n$ serve as weighting functions for the kinematic constraint. A suitable discretization of (15), (17) and the remaining constraints from (16) using a dual mortar finite element method is derived in Sect. 4 (see also [12,14,21,22]). There it will also be demonstrated how the additional nonlinearity stemming from contact (active set search) can be efficiently treated within an iterative Newton–Raphson framework.

2.4 Fluid–structure interface conditions

Dynamic and kinematic coupling conditions have to be fulfilled at the fluid–structure interface Γ_{FSI}, whose position varies with time. The direction of the interface normals is defined in Fig. 3. Note, that we focus on dry contact here: $\Gamma_{\text{FSI}} \cap \Gamma_c^{s,(1)} = \Gamma_{\text{FSI}} \cap \Gamma_c^{s,(2)} = \emptyset$. Obviously parts of the boundary change in time from being a fluid–structure interface to a contact interface and vice versa. Since we assume that no mass flow occurs across the interface, the normal velocities at the interface have to match each other

$$\boldsymbol{n}^f \cdot \boldsymbol{u} = -\boldsymbol{n}^s \cdot \dot{\boldsymbol{d}}^s \quad \text{on } \Gamma_{\text{FSI}}. \tag{18}$$

Viscous fluids require additionally a matching condition for tangential velocities, which completes the no slip-boundary conditions at the interface

$$\boldsymbol{u} = \dot{\boldsymbol{d}}^s \quad \text{on } \Gamma_{\text{FSI}}. \tag{19}$$

The force equilibrium requires the surface tractions to be equal

$$\boldsymbol{n}^f \cdot \boldsymbol{\sigma}^f = -\boldsymbol{n}^s \cdot \boldsymbol{\sigma}^s \quad \text{on } \Gamma_{\text{FSI}}. \tag{20}$$

The statement of the fluid–structure interface conditions completes the general problem description. In the following sections we derive a combined fluid–structure-contact interaction (FSCI) approach based on the above problem setup.

3 An XFEM based fluid–structure interaction formulation enabling topological changes

We start the development of the fluid–structure-contact method with a short review of the underlying XFEM FSI approach. Emphasis is put on details, which are important to understand the algorithmic combination with the contact formulation described in the next section. The interested reader is referred to [7–10,19,32,34] and references therein for further information about the XFEM FSI approach.

Figure 4 illustrates the applied two-field technique as well as the surface coupling between the fields. The fluid field and the structural field live on two distinct meshes: a fixed mesh for the fluid and moving Lagrangian meshes for the structure. The structure may move or deform arbitrarily in the background fluid mesh. Restrictions arise neither for the structural formulation nor for the integrated contact formulation. An exact fluid–structure interface representation allows to capture flow patterns around the structures with high accuracy and it enables also a straightforward combination of the FSI approach with the presented contact formulation.

3.1 Instationary Navier–Stokes equations including embedded Dirichlet conditions

Since the structural mesh can move and deform arbitrarily in a fixed background fluid mesh, the fluid–structure interface does not generally match with the fluid mesh. We apply a novel embedded Dirichlet formulation [9] to impose Dirichlet boundary conditions weakly on non-fitting grids as depicted in Figs. 4 and 5. The entire problem domain Ω is divided into a physical domain Ω^+, which is identical with the fluid domain Ω^f, and a completely fictitious domain Ω^-, which overlaps with the structural domain Ω^s. Initial conditions for velocity and pressure are tagged by a subscript zero in the physical domain and equal to zero in the fictitious domain. Since fluid field and structural field live on distinct meshes, we obtain two identical fluid–structure interfaces: the interface Γ_{FSI}^s belongs to the structural mesh and the interface $\Gamma_{\text{FSI}}^f = \Gamma^+$ to the fluid mesh. The structural interface velocity $\dot{\boldsymbol{d}}^s$ has to be imposed as an embedded Dirichlet condition on the velocity field $\boldsymbol{u}^+$ at the fluid interface. Formulating the Lagrange multiplier as traction or vector field living on the interface appeared to be a very hard task for three-dimensional problems. Instead, we introduce an additional stress field $\boldsymbol{\sigma}$ that lives in the fluid domain Ω^f and from which the surface traction is recovered by $\boldsymbol{n}^f \cdot \boldsymbol{\sigma}$. The corresponding test function to $\boldsymbol{\sigma}$ is $\boldsymbol{\gamma}$. The weak kinematic coupling along the fluid–structure interface is therefore given as

$$\left(\boldsymbol{n}^f \cdot \boldsymbol{\gamma}, \boldsymbol{u}^+ - \dot{\boldsymbol{d}}^s\right)_{\Gamma^+}. \tag{21}$$

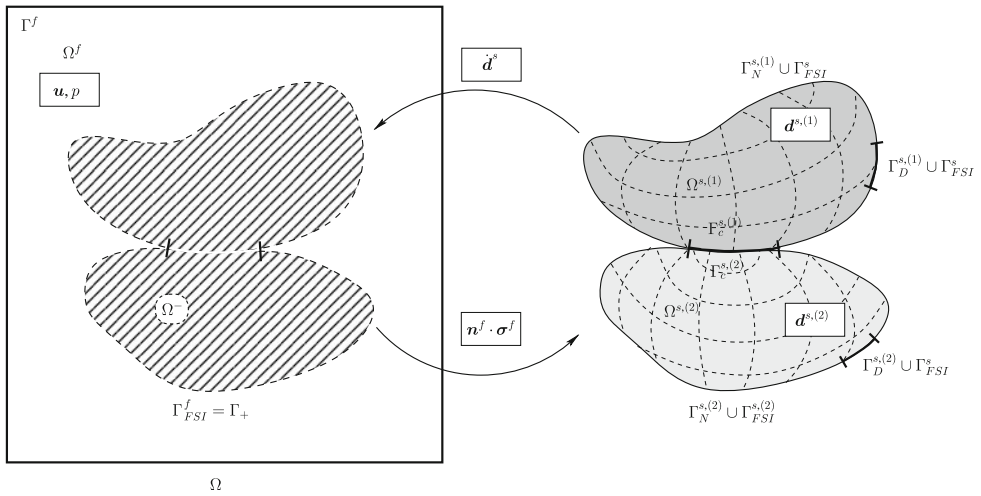

Fig. 4 Fluid–structure-contact interaction with coupling conditions

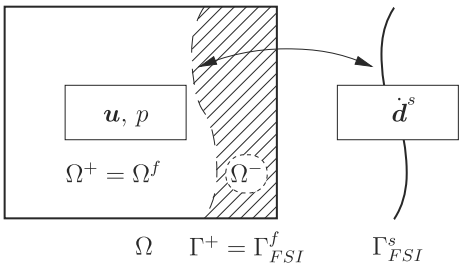

Fig. 5 Fluid domain with embedded Dirichlet boundary conditions on an interface which intersects the fluid domain

Substituting the traction vector by an additional unknown stress field $\boldsymbol{\sigma}$ leads to three equations for six unknowns. We formulate an additional strain rate balance $\boldsymbol{\epsilon}^s = \boldsymbol{\epsilon}^u$, to close the set of equations. The strain rate balance is enforced weakly only on elements, which are intersected by the interface. Both strain rates $\boldsymbol{\epsilon}^u$ and $\boldsymbol{\epsilon}^s$

$$\boldsymbol{\epsilon}^u = \frac{1}{2}\left(\nabla \boldsymbol{u} + (\nabla \boldsymbol{u})^T\right) \quad \text{and} \quad \boldsymbol{\epsilon}^s = \frac{1}{2\mu}(\boldsymbol{\sigma} + p\boldsymbol{I}), \tag{22}$$

as well as the stress tensors $\boldsymbol{\tau}^u = 2\mu\boldsymbol{\epsilon}^u$ and $\boldsymbol{\sigma}^u = -p\boldsymbol{I} + \boldsymbol{\tau}^u$ depend only on the primary unknowns $\boldsymbol{u}$, p and $\boldsymbol{\sigma}$.

Time-discretization of the strong form is derived here for the one-step-θ method, to keep the presentation simple. If no superscript is specified, the variable is computed at the new time step $n+1$, the superscript n refers to the old time step. The time-discretized strong form of the momentum equation results in

$$\begin{aligned}&\rho\boldsymbol{u} + \Delta t\theta\left[\rho\boldsymbol{u}\cdot\nabla\boldsymbol{u} - \nabla\cdot(-p\boldsymbol{I} + \boldsymbol{\tau}^u)\right]\\ &\quad -\rho\boldsymbol{u}^n - \Delta t(1-\theta)\rho\dot{\boldsymbol{u}}^n = \boldsymbol{0} \quad \text{in } \Omega^+.\end{aligned} \tag{23}$$

The embedded Dirichlet condition at the interface is also discretized

$$\boldsymbol{u}^+ - \frac{\boldsymbol{d}^s - \boldsymbol{d}^{s,n}}{\hat{\theta}\Delta t} + \frac{1-\hat{\theta}}{\hat{\theta}}\boldsymbol{u}^{+,n} = \boldsymbol{0} \quad \text{on } \Gamma^+. \tag{24}$$

to prepare for the coupling with the structural formulation. Note that the time-discretization of the Dirichlet boundary condition is not connected to the time-discretization of the momentum equation as expressed by different parameters θ and $\hat{\theta}$ (see also [5]). The structural displacements $\boldsymbol{d}^s$ and $\boldsymbol{d}^{s,n}$ are assumed to be prescribed for the time being, since only the fluid formulation is considered. Section 3.5 explains, how $\boldsymbol{d}^s$ and $\boldsymbol{d}^{s,n}$ are computed by coupling the structural formulation with the fluid formulation. More information about time integration in the context of this XFEM FSI approach is given in [10]. The weak form is obtained by testing with the velocity, pressure and stress test functions $\boldsymbol{v}$, q and $\boldsymbol{\gamma}$.

$$\begin{aligned}&(\boldsymbol{v}, \rho\boldsymbol{u})_{\Omega^+} + \Delta t\theta\Big[(\boldsymbol{v}, \rho\boldsymbol{u}\cdot\nabla\boldsymbol{u})_{\Omega^+} + \left(\nabla\boldsymbol{v}, -p\boldsymbol{I} + \boldsymbol{\tau}^u\right)_{\Omega^+}\\ &\quad + (q, \nabla\cdot\boldsymbol{u})_{\Omega^+} - \left(\boldsymbol{\gamma}, \frac{1}{2\nu}(\boldsymbol{\sigma} + p\boldsymbol{I}) - \boldsymbol{\epsilon}^u\right)_{\Omega^+}\\ &\quad - \left(\boldsymbol{n}^f\cdot\boldsymbol{\gamma}, \boldsymbol{u}\right)_{\Gamma^+} - \left(\boldsymbol{v}, \boldsymbol{n}^f\cdot\boldsymbol{\sigma}\right)_{\Gamma^+}\Big]\\ &= \left(\boldsymbol{v}, \rho\boldsymbol{u}^n + \Delta t(1-\theta)\rho\dot{\boldsymbol{u}}^n\right)_{\Omega^+}\\ &\quad + \Delta t\theta\left(\boldsymbol{v}, \bar{\boldsymbol{h}}\right)_{\Gamma_N^f} - \Delta t\theta\left(\boldsymbol{n}^f\cdot\boldsymbol{\gamma}, \frac{1}{\Delta t\hat{\theta}}\boldsymbol{d}^s - \frac{1}{\Delta t\hat{\theta}}\boldsymbol{d}^{s,n}\right)_{\Gamma^+}\\ &\quad + \Delta t\theta\left(\boldsymbol{n}^f\cdot\boldsymbol{\gamma}, \frac{1-\hat{\theta}}{\hat{\theta}}\boldsymbol{u}^{+,n}\right)_{\Gamma^+}\end{aligned} \tag{25}$$

In the following, we assume $\theta = \hat{\theta}$ to simplify the subsequent notation. One of the advantages of the proposed FSI approach is that standard fluid stabilization methods for the Navier–Stokes equation can be applied and that the stress based Lagrange multiplier does not require additional stabilization as demonstrated in [9]. We omit all fluid stabilization terms in this paper for brevity; the interested reader is referred to [10].

3.2 Geometric interface handling and enrichment strategies

The solution of the above derived weak form including embedded Dirichlet conditions requires an accurate localization of the structural interface in the background fluid mesh as well as an integrable surface representation of the interface in each fluid element. A detailed description of the interface handling algorithm is given in [17] and [19]. In summary, the structural boundary is localized in each fluid element and the resulting part of the interface is triangulated. The fluid element including the triangulated interface part is subtetrahedralized based on a Constrained Delaunay Tetrahedralization. The collection of tetrahedral volume cells in the intersected fluid element allows for a numerically exact integration of the fluid part of an intersected volume element. The fluid–structure interface can be integrated numerically by the triangulated interface representation. The algorithm is applicable to hexahedral elements, tetrahedral elements, wedges or any other element types also of different order and it can handle several interfaces in a single fluid element.

The sharp interface description within an element is based on the eXtended finite element method (XFEM) proposed to model an arbitrary discontinuity or interface within a single element by enriching the ansatz function space. It was initially developed for discontinuous solid mechanics problems such as crack growths in [2] and [20].

The physical field is approximated by the sum of a continuous term and a discontinuous term. The latter term introduces additional degrees of freedom. The interpolation function in the discontinuous term consists of a product of shape functions and a discontinuous enrichment function. According to the underlying physics that we have to model, we choose the well-known Heaviside function as enrichment function, such that it equals one in the fluid domain and zero in the fictitious part occupied by the structure

$$\Psi(\boldsymbol{x}) = \begin{cases} +1 & \text{in } \Omega^+ \\ 0 & \text{in } \Omega^- \end{cases} . \tag{26}$$

The following equation represents schematically the trial and test functions for velocity $\boldsymbol{u}$ and $\boldsymbol{v}$, pressure p and q, as well as stress $\boldsymbol{\sigma}$ and $\boldsymbol{\gamma}$. As explained above, each quantity is approximated by a continuous term and a discontinuous term based on the product of usual shape functions N and enrichment function Ψ. The continuous term is tagged by a superscript c and the discontinuous term by dc.

$$(\cdot)^h(\boldsymbol{x},t) = \sum_I N_I(\boldsymbol{x})(\cdot)_I^c(t) + \sum_J N_J(\boldsymbol{x})\Psi(\boldsymbol{x})(\cdot)_J^{dc}(t). \tag{27}$$

We apply linear or quadratic equal order shape functions N, which are continuous at element boundaries for velocity and pressure discretization and discontinuous at element boundaries for stress discretization.

3.3 Discrete matrix formulation

The discrete matrix formulation is obtained by inserting trial and test functions into the weak formulation (25).

The matrix $\boldsymbol{K}_{uu}$ denotes the sum of the standard operators for mass, convection and viscous stresses $\boldsymbol{K}_{uu} = \boldsymbol{M}_{uu} + \boldsymbol{N}_{uu} + \boldsymbol{V}_{uu}$ with

$$\boldsymbol{M}_{uu} : +(\boldsymbol{v}, \rho\boldsymbol{u})_{\Omega^+} , \tag{28}$$

$$\boldsymbol{N}_{uu} : +\Delta t\theta\, (\boldsymbol{v}, \rho\boldsymbol{u}\cdot\nabla\boldsymbol{u})_{\Omega^+} , \tag{29}$$

$$\boldsymbol{V}_{uu} : +\Delta t\theta \left(\nabla\boldsymbol{v}, \boldsymbol{\tau}^u\right)_{\Omega^+} . \tag{30}$$

Gradient and divergence matrices are obtained as

$$\boldsymbol{K}_{up} : -\Delta t\theta\, (\nabla\boldsymbol{v}, p\boldsymbol{I})_{\Omega^+} , \tag{31}$$

$$\boldsymbol{K}_{pu} : +\Delta t\theta\, (q, \nabla\cdot\boldsymbol{u})_{\Omega^+} . \tag{32}$$

Stabilization leads to the matrix $\boldsymbol{K}_{pp}$. The following domain and boundary integrals result form the introduced stress field $\boldsymbol{\sigma}$ and the test function $\boldsymbol{\gamma}$. Matrices related to domain integrals are denoted by

$$\boldsymbol{K}_{\sigma u} : +\Delta t\theta \left(\boldsymbol{\gamma}, \boldsymbol{\epsilon}^u\right)_{\Omega^+} , \tag{33}$$

$$\boldsymbol{K}_{\sigma p} : -\Delta t\theta \left(\boldsymbol{\gamma}, \frac{1}{2\nu} p\boldsymbol{I}\right)_{\Omega^+} , \tag{34}$$

$$\boldsymbol{K}_{\sigma\sigma} : -\Delta t\theta \left(\boldsymbol{\gamma}, \frac{1}{2\nu}\boldsymbol{\sigma}\right)_{\Omega^+} . \tag{35}$$

Matrices corresponding to boundary integrals are written as

$$\boldsymbol{G}_{u\sigma} : -\Delta t\theta \left(\boldsymbol{v}, \boldsymbol{n}^f\cdot\boldsymbol{\sigma}\right)_{\Gamma^+} , \tag{36}$$

$$\boldsymbol{G}_{\sigma u} : -\Delta t\theta \left(\boldsymbol{n}^f\cdot\boldsymbol{\gamma}, \boldsymbol{u}\right)_{\Gamma^+} , \tag{37}$$

$$\boldsymbol{G}_{\sigma u^n} : -\Delta t(1-\theta) \left(\boldsymbol{n}^f\cdot\boldsymbol{\gamma}, \boldsymbol{u}^n\right)_{\Gamma^+} , \tag{38}$$

$$\boldsymbol{G}_{\sigma d^s} : -\left(\boldsymbol{n}^f\cdot\boldsymbol{\gamma}, \boldsymbol{d}^s\right)_{\Gamma^+} , \tag{39}$$

$$\boldsymbol{G}_{\sigma d^{s,n}} : +\left(\boldsymbol{n}^f\cdot\boldsymbol{\gamma}, \boldsymbol{d}^{s,n}\right)_{\Gamma^+} . \tag{40}$$

The right-hand side vectors $\boldsymbol{f}^{rhs}$ and $\boldsymbol{f}^{rhs,\sigma}$ are related to

$$\begin{aligned} \boldsymbol{f}^{rhs} : \quad & +\left(\boldsymbol{v}, \rho\boldsymbol{u}^n + \Delta t(1-\theta)\rho\dot{\boldsymbol{u}}^n\right)_{\Omega^+} \\ & +\Delta t\theta(\boldsymbol{v}, \bar{\boldsymbol{h}})_{\Gamma^N}, \end{aligned} \tag{41}$$

$$\begin{aligned} \boldsymbol{f}^{rhs,\sigma} : \quad & +\left(\boldsymbol{n}^f\cdot\boldsymbol{\gamma}, \boldsymbol{d}^{s,n}\right)_{\Gamma^+} \\ & -\Delta t(1-\theta)\left(\boldsymbol{n}^f\cdot\boldsymbol{\gamma}, \boldsymbol{u}^n\right)_{\Gamma^+} . \end{aligned} \tag{42}$$

The discrete matrix formulation with a prescribed interface velocity may be written as

$$\begin{bmatrix} \boldsymbol{K}_{uu} & \boldsymbol{K}_{up} & \boldsymbol{G}_{u\sigma} \\ \boldsymbol{K}_{pu} & \boldsymbol{K}_{pp} & \boldsymbol{0} \\ \boldsymbol{K}_{\sigma u}+\boldsymbol{G}_{\sigma u} & \boldsymbol{K}_{\sigma p} & \boldsymbol{K}_{\sigma\sigma} \end{bmatrix} \begin{bmatrix} \boldsymbol{u} \\ \boldsymbol{p} \\ \boldsymbol{\sigma} \end{bmatrix} = \begin{bmatrix} \boldsymbol{f}^{rhs} \\ \boldsymbol{0} \\ \boldsymbol{G}_{\sigma d^s}\boldsymbol{d}^s + \boldsymbol{f}^{rhs,\sigma} \end{bmatrix} . \tag{43}$$

To prepare for coupling with the structural formulation, we extract the displacements $\boldsymbol{d}^s$ and include it in the solution vector. The resulting matrix formulation

$$\begin{bmatrix} \boldsymbol{K}_{uu} & \boldsymbol{K}_{up} & \boldsymbol{G}_{u\sigma} & \boldsymbol{0} \\ \boldsymbol{K}_{pu} & \boldsymbol{K}_{pp} & \boldsymbol{0} & \boldsymbol{0} \\ \boldsymbol{K}_{\sigma u}+\boldsymbol{G}_{\sigma u} & \boldsymbol{K}_{\sigma p} & \boldsymbol{K}_{\sigma\sigma} & -\boldsymbol{G}_{\sigma d^s} \\ \square & \square & \square & \square \end{bmatrix} \begin{bmatrix} \boldsymbol{u} \\ \boldsymbol{p} \\ \boldsymbol{\sigma} \\ \boldsymbol{d}^s \end{bmatrix} = \begin{bmatrix} \boldsymbol{f}^{rhs} \\ \boldsymbol{0} \\ \boldsymbol{f}^{rhs,\sigma} \\ \square \end{bmatrix}. \tag{44}$$

contains the entire fluid description including matrices resulting from the additional stress field $\boldsymbol{\sigma}$, which can be condensed on the element level as demonstrated in Sect. 5. The missing structural equation as well as the coupling matrix that results from imposing fluid stresses onto the structure is derived in Sect. 3.5. In the meanwhile, we tag the missing vector and matrices by boxes $\square$ in system (44).

3.4 Linearization

In this subsection, we derive the linearized coupled system for fluid flows interacting with a structural interface based on embedded Dirichlet conditions. We restrict the derivation to a very schematic representation of the individual derivatives and assume $\theta = 1.0$ for simplicity.

The residual $\mathcal{R}^u(\boldsymbol{u}, \boldsymbol{p}, \boldsymbol{\sigma})$ of the first equation in the discrete system (44) may be written as

$$\begin{aligned} \mathcal{R}^u(\boldsymbol{u}, \boldsymbol{p}, \boldsymbol{\sigma}) = \boldsymbol{f}^{rhs} &- \frac{1}{\Delta t}\boldsymbol{M}_{uu}\boldsymbol{u} - \boldsymbol{N}_{uu}(\boldsymbol{u})\boldsymbol{u} \\ &- \boldsymbol{V}_{uu}\boldsymbol{u} - \boldsymbol{K}_{up}\boldsymbol{p} - \boldsymbol{G}_{u\sigma}\boldsymbol{\sigma} = \boldsymbol{0}. \end{aligned} \tag{45}$$

The residual of the second equation denoted by $\mathcal{R}^p(\boldsymbol{u}, \boldsymbol{p})$ is

$$\mathcal{R}^p(\boldsymbol{u}, \boldsymbol{p}) = -\boldsymbol{K}_{pu}\boldsymbol{u} - \boldsymbol{K}_{pp}\boldsymbol{p} = \boldsymbol{0}. \tag{46}$$

The residual $\mathcal{R}^\sigma(\boldsymbol{u}, \boldsymbol{p}, \boldsymbol{\sigma}, \boldsymbol{d}^s)$ due to the additional stress field $\boldsymbol{\sigma}$ results in

$$\begin{aligned} \mathcal{R}^\sigma(\boldsymbol{u}, \boldsymbol{p}, \boldsymbol{\sigma}, \boldsymbol{d}^s) = \boldsymbol{f}^{rhs,\sigma} &+ \boldsymbol{G}_{\sigma d}\boldsymbol{d}^s - (\boldsymbol{K}_{\sigma u} + \boldsymbol{G}_{\sigma u})\boldsymbol{u} \\ &- \boldsymbol{K}_{\sigma p}\boldsymbol{p} - \boldsymbol{K}_{\sigma\sigma}\boldsymbol{\sigma} = \boldsymbol{0}. \end{aligned} \tag{47}$$

The structural momentum equation is not yet included, but will be considered in the next subsection.

Each residual is developed in a Taylor series in $\boldsymbol{u}$, $\boldsymbol{p}$, $\boldsymbol{\sigma}$ and $\boldsymbol{d}^s$ up to first order as usual.

The resulting directional derivatives

$$\boldsymbol{L}_{xy} = \left.\frac{\partial \mathcal{R}^x}{\partial \boldsymbol{y}}\right|_{\boldsymbol{y}} \tag{48}$$

determine the individual subblocks of the system matrix for the linearized coupled system of equations including the fluid description and embedded Dirichlet conditions

$$\begin{bmatrix} \boldsymbol{L}_{uu} & \boldsymbol{L}_{up} & \boldsymbol{L}_{u\sigma} & \boldsymbol{0} \\ \boldsymbol{L}_{pu} & \boldsymbol{L}_{pp} & \boldsymbol{0} & \boldsymbol{0} \\ \boldsymbol{L}_{\sigma u} & \boldsymbol{L}_{\sigma p} & \boldsymbol{L}_{\sigma\sigma} & \boldsymbol{L}_{\sigma d} \\ \square & \square & \square & \square \end{bmatrix} \begin{bmatrix} \Delta\boldsymbol{u} \\ \Delta\boldsymbol{p} \\ \Delta\boldsymbol{\sigma} \\ \Delta\boldsymbol{d}^s \end{bmatrix} = \begin{bmatrix} -\mathcal{R}^u \\ -\mathcal{R}^p \\ -\mathcal{R}^\sigma \\ \square \end{bmatrix}. \tag{49}$$

The right-hand side contains the residuals.

3.5 Structural discretization

Discretization of the weak form (12) is based on standard (often mixed/hybrid) finite element discretization that is abundantly discussed in literature and thus will not be detailed here. We begin with a reformulation of the structural weak form by including Neumann type boundary conditions arising from fluid stresses. The Neumann boundary is split into a usual Neumann boundary Γ^s_N and the fluid–structure interface of Neumann type Γ^s_{FSI}. The traction force $\bar{\boldsymbol{h}}^s_{\mathrm{FSI}}$ arises from the fluid stresses, expressed by the additional stress field $\boldsymbol{\sigma}^f$ at the fluid–structure interface Γ^s_{FSI}

$$\bar{\boldsymbol{h}}^s_{\mathrm{FSI}} = -\boldsymbol{n}^f \cdot \boldsymbol{\sigma}^f \quad \text{on } \Gamma^s_{\mathrm{FSI}}. \tag{50}$$

Note that we tag the additional fluid stress field with a superscript f here to avoid confusion. The resulting weak form may be written as

$$\begin{aligned} &(\delta\boldsymbol{d}^s, \rho^s\ddot{\boldsymbol{d}}^s)_{\Omega^s} + (\nabla\delta\boldsymbol{d}^s, \boldsymbol{\sigma}^s)_{\Omega^s} - (\delta\boldsymbol{d}^s, \boldsymbol{b}^s)_{\Omega^s} \\ &\quad - (\delta\boldsymbol{d}^s, \bar{\boldsymbol{h}}^s)_{\Gamma^s_N} - (\delta\boldsymbol{d}^s, \bar{\boldsymbol{h}}^s_{\mathrm{FSI}})_{\Gamma^s_{\mathrm{FSI}}} = 0. \end{aligned} \tag{51}$$

For presentation, a β-Newmark scheme with integration parameters β and γ is applied as implicit time integration scheme. Note that this scheme is not stable in the nonlinear case. The actual implementation is based on generalized-α time integration shifting evaluation of the discretized equations of motion to generalized mid-points [3]. Displacement time derivatives are discretized as follows

$$\ddot{\boldsymbol{d}}^{s,n+1} = \frac{1}{\beta\Delta t^2}\left(\boldsymbol{d}^{s,n+1} - \boldsymbol{d}^{s,n}\right) - \frac{1}{\beta\Delta t}\dot{\boldsymbol{d}}^{s,n} - \frac{1-2\beta}{2\beta}\ddot{\boldsymbol{d}}^{s,n} \tag{52}$$

$$\dot{\boldsymbol{d}}^{s,n+1} = \dot{\boldsymbol{d}}^{s,n} + \gamma\Delta t\ddot{\boldsymbol{d}}^{s,n+1} + (1-\gamma)\Delta t\ddot{\boldsymbol{d}}^{s,n}. \tag{53}$$

Defining a mass matrix $\boldsymbol{M}$ and inserting (52) and (53) into the usual semi-discrete equations of motion yields the fully discretized expression

$$\begin{aligned} &\frac{1}{\beta\Delta t^2}\boldsymbol{M}\boldsymbol{d}^{s,n+1} + \boldsymbol{f}_{int}(\boldsymbol{d}^{s,n+1}) \\ &\quad = \boldsymbol{f}^{n+1}_{ext,N} + \boldsymbol{f}_{\mathrm{FSI}}(\boldsymbol{\sigma}^{f,n+1}) \\ &\quad\quad + \underbrace{\boldsymbol{M}\left(\frac{1}{\beta\Delta t^2}\boldsymbol{d}^{s,n} + \frac{1}{\beta\Delta t}\dot{\boldsymbol{d}}^{s,n} + \frac{1-2\beta}{2\beta}\ddot{\boldsymbol{d}}^{s,n}\right)}_{\boldsymbol{f}^{n+1}_{dyn}}, \end{aligned} \tag{54}$$

where $\boldsymbol{d}^{s,n+1}$ now represents the *discrete* vector of structural nodal displacements. The force term $\boldsymbol{f}_{\mathrm{FSI}}(\boldsymbol{\sigma}^{f,n+1})$ depending on the fluid stress $\boldsymbol{\sigma}^{f,n+1}$ will introduce the missing linearized coupling matrix $\boldsymbol{L}_{d\sigma}$.

Consistent linearization within a Newton–Raphson framework leads to the following linear system of equations to be solved in the ith iteration step

$$\boldsymbol{L}_{d\sigma}|_i^{n+1}\,\Delta\boldsymbol{\sigma}_i^{f,n+1} + \boldsymbol{L}_{dd}|_i^{n+1}\,\Delta\boldsymbol{d}_i^{s,n+1} = -\mathcal{R}^d(\boldsymbol{\sigma}^f,\boldsymbol{d}^s)|_i^{n+1}. \tag{55}$$

The iteration index i will be dropped further on for brevity. The effective force residual $\mathcal{R}^d(\boldsymbol{\sigma}^f,\boldsymbol{d}^s)$ may be written as

$$\mathcal{R}^d(\boldsymbol{\sigma}^f,\boldsymbol{d}^s) = \frac{1}{\beta\Delta t^2}\boldsymbol{M}\boldsymbol{d}^{s,n+1} + \boldsymbol{f}_{int}(\boldsymbol{d}^{s,n+1}) - \boldsymbol{f}_{ext,N}^{n+1} - \boldsymbol{f}_{\mathrm{FSI}}(\boldsymbol{\sigma}^{f,n+1}) - \boldsymbol{f}_{dyn}^{n+1}. \tag{56}$$

The effective tangent stiffness matrix $\boldsymbol{L}_{dd}$ and the coupling matrix $\boldsymbol{L}_{d\sigma}$ are derived as

$$\boldsymbol{L}_{dd} = \left(\frac{1}{\beta\Delta t^2}\boldsymbol{M} + \boldsymbol{K}_T\right) \quad \text{with} \quad \boldsymbol{K}_T = \frac{\partial \boldsymbol{f}_{int}}{\partial \boldsymbol{d}^{s,n+1}},$$
$$\boldsymbol{L}_{d\sigma} = -\frac{\partial \boldsymbol{f}_{\mathrm{FSI}}}{\partial \boldsymbol{\sigma}^{f,n+1}}. \tag{57}$$

The final monolithic fluid–structure interaction system can then be written as

$$\begin{bmatrix} \boldsymbol{L}_{uu} & \boldsymbol{L}_{up} & \boldsymbol{L}_{u\sigma} & \boldsymbol{0} \\ \boldsymbol{L}_{pu} & \boldsymbol{L}_{pp} & \boldsymbol{0} & \boldsymbol{0} \\ \boldsymbol{L}_{\sigma u} & \boldsymbol{L}_{\sigma p} & \boldsymbol{L}_{\sigma\sigma} & \boldsymbol{L}_{\sigma d} \\ \boldsymbol{0} & \boldsymbol{0} & \boldsymbol{L}_{d\sigma} & \boldsymbol{L}_{dd} \end{bmatrix} \begin{bmatrix} \Delta\boldsymbol{u} \\ \Delta\boldsymbol{p} \\ \Delta\boldsymbol{\sigma} \\ \Delta\boldsymbol{d}^s \end{bmatrix} = \begin{bmatrix} -\mathcal{R}^u \\ -\mathcal{R}^p \\ -\mathcal{R}^\sigma \\ -\mathcal{R}^d \end{bmatrix}. \tag{58}$$

In the upcoming paragraph, when considering a dual mortar discretization for structural contact, the fourth line of (58) will be extended. Discrete contact forces enter the effective force residual $\mathcal{R}^d$, and the tangent stiffness $\boldsymbol{L}_{dd}$ is modified by taking into account contact stiffness terms. It is important to point out that this makes the consideration of contact almost fully self-contained, meaning that no algorithmic changes to the general FSI setup become necessary.

4 Dual mortar contact discretization

4.1 Discretization of contact virtual work

Spatial discretization of contact virtual work (15) and contact constraints (16) and (17) requires a discretization of slave and master surface, which is simply obtained based on their trace space relationship with the underlying structural discretization. We consider 3D first-order Lagrangian finite elements here and shape functions for the contact surface discretization follow directly from the shape functions on $\Omega^{s,(i)h}$, $i = 1, 2$. Thus, contact surfaces may consist of 3-node triangular and 4-node quadrilateral elements. Accordingly, the following general form of slave and master displacement interpolation (and in full analogy for geometry interpolation owing to the isoparametric concept) holds

$$\boldsymbol{d}^{s,(1)h}|_{\Gamma_c^{s,(1)h}} = \sum_{k=1}^{n_{sl}} N_k^{(1)}(\boldsymbol{\xi}^{(1)})\,\boldsymbol{d}_k^{s,(1)}, \tag{59}$$

$$\boldsymbol{d}^{s,(2)h}|_{\Gamma_c^{s,(2)h}} = \sum_{l=1}^{n_m} N_l^{(2)}(\boldsymbol{\xi}^{(2)})\,\boldsymbol{d}_l^{s,(2)}, \tag{60}$$

with the total number of slave and master nodes, n_{sl} and n_m, respectively. Nodal displacements are given by $\boldsymbol{d}_k^{s,(1)}$, $\boldsymbol{d}_l^{s,(2)}$ and shape functions $N_k^{(1)}$, $N_l^{(2)}$ are defined with respect to a suitable finite element parameter space $\boldsymbol{\xi}^{(i)} = (\xi^{(i)}, \eta^{(i)})$. Lagrange multiplier interpolation on the slave surface is based on so-called dual shape functions Φ_j [35] as

$$\boldsymbol{\lambda}^h = \sum_{j=1}^{n_{sl}} \Phi_j(\boldsymbol{\xi}^{(1)})\boldsymbol{z}_j, \tag{61}$$

with discrete nodal Lagrange multipliers $\boldsymbol{z}_j$. The polynomial degree of these dual shape functions is chosen identical to the polynomial degree of the surface geometry interpolation. Moreover, they are constructed such that a biorthogonality condition as introduced in [14,35,36] holds (for brevity, the discretized slave surface is denoted as Γ_c^h in the following)

$$\int_{\Gamma_c^h} \Phi_j(\boldsymbol{\xi}^{(1)})\,N_k^{(1)}(\boldsymbol{\xi}^{(1)})\,\mathrm{d}\gamma = \delta_{jk}\int_{\Gamma_c^h} N_k^{(1)}(\boldsymbol{\xi}^{(1)})\,\mathrm{d}\gamma, \tag{62}$$

where δ_{jk} is the Kronecker delta. As can be demonstrated easily, this choice is very advantageous for the presented approach, as it allows for static condensation of the discrete multipliers $\boldsymbol{z}_j$. It is worth mentioning that an a priori definition of dual shape functions in the context of finite deformations is in general not possible, as the biorthogonality relation (62) is deformation-dependent. For an overview and exemplary local calculations of element-specific dual shape functions in 3D contact analysis we refer to [12] and [22]. When substituting displacement and Lagrange multiplier interpolation into contact virtual work expression (15), the nodal blocks of two mortar integral matrices $\boldsymbol{D} \in \mathbb{R}^{3n_{sl}\times 3n_{sl}}$ and $\boldsymbol{M} \in \mathbb{R}^{3n_{sl}\times 3n_m}$ emerge as

$$\boldsymbol{D}[j,j] = D_{jj}\,\boldsymbol{I}_3 = \int_{\Gamma_c^h} N_j^{(1)}\mathrm{d}\gamma\;\boldsymbol{I}_3, \tag{63}$$

$$\boldsymbol{M}[j,l] = M_{jl}\,\boldsymbol{I}_3 = \int_{\Gamma_c^h} \Phi_j N_l^{(2)}\mathrm{d}\gamma\;\boldsymbol{I}_3, \tag{64}$$

with $j = 1,\ldots,n_{sl}$, $l = 1,\ldots,n_m$ and with the identity $\boldsymbol{I}_3 \in \mathbb{R}^{3\times 3}$. Biorthogonality relation (62) has allowed for the beneficial simplification of $\boldsymbol{D}$ to become a diagonal matrix here. Finally, an algebraic notation of the discretized contact virtual work

$$\delta\Pi_c^h = \left(\delta \boldsymbol{d}^{s,(1)}\right)^T \boldsymbol{D}\,\boldsymbol{z} - \left(\delta \boldsymbol{d}^{s,(2)}\right)^T \boldsymbol{M}^T\,\boldsymbol{z} \tag{65}$$

is obtained, where all discrete nodal values of Lagrange multipliers and nodal test function values are assembled into global vectors $\boldsymbol{z}$, $\delta\boldsymbol{d}^{s,(1)}$ and $\delta\boldsymbol{d}^{s,(2)}$, respectively. To make algebraic representations clearer, all finite element nodes in the two domains $\Omega^{s,(1)h}$ and $\Omega^{s,(2)h}$ are split into three subsets: a subset $\mathcal{S}$ containing all n_{sl} potential slave side contact nodes, a subset $\mathcal{M}$ of all n_m potential master side contact nodes and the set of all remaining nodes $\mathcal{N}$. The global nodal displacement vector can be sorted accordingly, yielding $\boldsymbol{d}^s = (\boldsymbol{d}^s_{\mathcal{N}}, \boldsymbol{d}^s_{\mathcal{M}}, \boldsymbol{d}^s_{\mathcal{S}})^T$. Then, the vector of discrete contact forces is

$$\boldsymbol{f}_c = [\boldsymbol{0} \quad -\boldsymbol{M} \quad \boldsymbol{D}]^T\,\boldsymbol{z}. \tag{66}$$

As described earlier, the contact forces extend the fully discretized force residual $\mathcal{R}^d$ defined in (55) leading to the following modified residual including contact

$$\mathcal{R}^{dc} = \mathcal{R}^d + \boldsymbol{f}_c(\boldsymbol{d}^{s,n+1}). \tag{67}$$

4.2 Discretization of contact constraints

A discrete version of the weak non-penetration condition is obtained by inserting the Lagrange multiplier interpolation (61) into (17)

$$\int_{\Gamma_c^{s,(1)}} \delta\lambda_n\, g\, \mathrm{d}\gamma \approx \sum_{j=1}^{n_{sl}} (\delta z_n)_j \int_{\Gamma_c^h} \Phi_j\, \hat{g}\, \mathrm{d}\gamma \geq 0. \tag{68}$$

Here, $\hat{g}$ is the discrete version of the gap function defined in (14). Introducing for each slave node $j \in \mathcal{S}$ a discrete normal weighted gap $\tilde{g}_j$ yields

$$\tilde{g}_j = \int_{\Gamma_c^h} \Phi_j\, \hat{g}\, \mathrm{d}\gamma \geq 0. \tag{69}$$

The discrete nodal values $\boldsymbol{z}_j \in \mathbb{R}^3$, $j = 1, \ldots, n_{sl}$ of the Lagrange multipliers are split into normal and tangential components $(z_n)_j \boldsymbol{n}_j^c$ and $(z_\tau^\xi)_j \boldsymbol{\tau}_j^\xi$, $(z_\tau^\eta)_j \boldsymbol{\tau}_j^\eta$, respectively. Here $\boldsymbol{n}_j^c$, $\boldsymbol{\tau}_j^\xi$ and $\boldsymbol{\tau}_j^\eta$ are the unit normal and tangent vectors at slave node j. Summarizing the discrete formulation of the KKT conditions yields

$$\tilde{g}_j \geq 0, \quad (z_n)_j \geq 0, \quad (z_n)_j \tilde{g}_j = 0. \tag{70}$$

The frictionless sliding conditions are discretized as

$$(z_\tau^\xi)_j = (z_\tau^\eta)_j = 0. \tag{71}$$

4.3 Evaluation of mortar integrals and weighted gaps

In order to evaluate the discrete mortar integral terms (63), (64) and discrete weighted gaps (69), one has to set up so-called contact segments suitable for numerical integration. As the main focus of this paper is on the integration of the presented contact formulation into a 3D XFEM FSI framework, the numerical integration of contact expressions is not discussed here, but only outlined schematically.

A prerequisite for any mortar coupling and interface segmentation method is the definition of a suitable contact normal $\boldsymbol{n}^c$. While not unique, the continuous field of slave normals based on nodal averaging first suggested in [39] has proven to provide the desired robustness for mortar contact methods [21,22]. For details on the numerical integration algorithms in both 2D and 3D the interested reader is referred to the original work by Puso et al. [23–25] and to the authors' recent work on dual mortar contact [21,22].

4.4 Semi-smooth Newton approach

The discrete contact constraints (70) are still stated as inequalities and thus require a suitable active set strategy as solution technique. The idea of any active set strategy is to find the correct subset of all slave nodes which are currently in contact with the master surface. The set $\mathcal{A} \subseteq \mathcal{S}$ is called the active set and definition of the inactive set $\mathcal{I} = \mathcal{S} \backslash \mathcal{A}$ is straightforward.

As demonstrated recently in [21] and [22] for both 2D and 3D, the idea of an active set strategy can be successfully merged with the idea of a semi-smooth Newton method in the context of finite deformations. The main advantage of this approach is the fact that all sources of nonlinearities, i.e. finite deformations, nonlinear material behavior and contact itself, can be treated within one single iterative scheme. There is no need for a nested approach with the outer loop solving for the correct active set as e.g. in [12].

We start with a reformulation of the discrete KKT-conditions (70) within one single complementarity function C_j for each slave node $j \in \mathcal{S}$ as

$$C_j\left(\boldsymbol{z}_j, \boldsymbol{d}^s\right) = (z_n)_j - \max\left(0, (z_n)_j - c_n \tilde{g}_j\right) = 0, \quad c_n > 0. \tag{72}$$

It can be easily shown that (72) is equivalent to the set of KKT-conditions and that this equivalence holds for arbitrary positive values of the complementarity parameter c_n. While C_j is a continuous function, it is non-smooth and has no uniquely defined derivative at positions $(z_n)_j - c_n \tilde{g}_j = 0$. Yet, it is well-known from mathematical literature on constrained optimization [13,26] that the *max*-function is semi-smooth and therefore a Newton method can still be applied.

4.5 Consistent linearization

Defining as generalized derivative of the *max*-function

$$f(x) = \max(a, x) \longrightarrow \Delta f(x) = \begin{cases} 0 & \text{if } x \leq a \\ 1 & \text{if } x > a \end{cases}, \tag{73}$$

one can perform a semi-smooth Newton step at the current iterate i to be solved for the primal-dual pair of discrete variables $(\boldsymbol{d}^s_{i+1}, z_{i+1})$, with

$$\Delta(\cdot) = \frac{\partial(\cdot)}{\partial \boldsymbol{d}^s} \Delta \boldsymbol{d}^s. \tag{74}$$

Strictly speaking, full linearization $\Delta(\cdot)$ also comprises directional derivatives with respect to the discrete Lagrange multipliers z. However, apart from the active set decision contained in (72) and linearized in (73), all contact terms are at most linear in z and thus can be directly expressed in terms of z_{i+1}. Consistent linearization of the involved quantities, such as the discrete contact forces $\boldsymbol{f}_c$, the mortar matrices $\boldsymbol{D}$ and $\boldsymbol{M}$ and the discrete weighted gaps $\tilde{g}_j$ has been presented in great detail in [21] for 2D and in [22] for 3D. Here we just summarize the resulting semi-smooth Newton algorithm to be solved within one time increment $t^n \to t^{n+1}$. As in Sect. 3.5, simple β-Newmark time integration is assumed for presentation. As all quantities are evaluated at t^{n+1}, the superscript $n+1$ is omitted.

Algorithm 1

1. Set $i = 0$ and initialize the solution $(\boldsymbol{d}^s_0, z_0)$
2. Initialization: $\mathcal{A}_0 \cup \mathcal{I}_0 = \mathcal{S}$ and $\mathcal{A}_0 \cap \mathcal{I}_0 = \emptyset$
3. Find the primal-dual pair $(\Delta \boldsymbol{d}^s_i, z_{i+1})$ by solving

$$\Delta \mathcal{R}^{dc}|_i = -\mathcal{R}^{dc}|_i, \tag{75}$$

$$z_j|_{i+1} = 0 \quad \forall j \in \mathcal{I}_i, \tag{76}$$

$$\Delta \tilde{g}_j|_i = -\tilde{g}_j|_i \quad \forall j \in \mathcal{A}_i, \tag{77}$$

$$\Delta \boldsymbol{\tau}^{\xi}_j \cdot z_j|_i + \boldsymbol{\tau}^{\xi}_j \cdot z_j|_{i+1} = 0 \quad \forall j \in \mathcal{A}_i, \tag{78}$$

$$\Delta \boldsymbol{\tau}^{\eta}_j \cdot z_j|_i + \boldsymbol{\tau}^{\eta}_j \cdot z_j|_{i+1} = 0 \quad \forall j \in \mathcal{A}_i. \tag{79}$$

4. Update $\boldsymbol{d}^s_{i+1} = \boldsymbol{d}^s_i + \Delta \boldsymbol{d}^s_i$
5. Set $\mathcal{A}_{i+1}$ and $\mathcal{I}_{i+1}$ to

$$\begin{aligned} \mathcal{A}_{i+1} &:= \left\{ j \in \mathcal{S} \,|\, (z_n)_j|_{i+1} - c_n \tilde{g}_j|_{i+1} > 0 \right\}, \\ \mathcal{I}_{i+1} &:= \left\{ j \in \mathcal{S} \,|\, (z_n)_j|_{i+1} - c_n \tilde{g}_j|_{i+1} \leq 0 \right\}. \end{aligned} \tag{80}$$

6. If $\mathcal{A}_{i+1} = \mathcal{A}_i$, $\mathcal{I}_{i+1} = \mathcal{I}_i$ and $\|\mathcal{R}^{tot}\| \leq \epsilon_r$, then stop, else set $i := i + 1$ and go to step (3).

The variable ϵ_r denotes an absolute Newton convergence tolerance for the $\mathcal{L}^2$-norm of the total residual vector $\mathcal{R}^{tot}$, which comprises the force residual $\mathcal{R}^{dc}$ and the residual of the contact constraints (76)–(79). All types of nonlinearities including the search for the correct active set are resolved within one Newton iteration, with the sets $\mathcal{I}_i$ and $\mathcal{A}_i$ being updated after each semi-smooth Newton step. Numerical tests reveal that even for large step sizes and fine contacting meshes the correct active set is found after a few Newton steps. Once the sets remain constant, quadratic convergence is obtained due to the underlying fully consistent linearization. An algebraic representation of the linear system (75)–(79) to be solved in each semi-smooth Newton step has been presented in [21,22]. Owing to the dual shape functions introduced for the Lagrange multipliers in Sect. 4.1, the matrix $\boldsymbol{D}$ becomes diagonal making its inversion trivial. The discrete multiplier values can be eliminated by condensation and the resulting linear system of equations thus contains *only displacement degrees of freedom* and is *positive definite*. An undesirable increase in global system size due to the Lagrange multiplier degrees of freedom is avoided. Here, we restrict the presentation to a schematic algebraic form

$$\boldsymbol{L}_{d\sigma}|^{n+1}_i \, \Delta \boldsymbol{\sigma}^{f,n+1}_i + \tilde{\boldsymbol{L}}_{dd}|^{n+1}_i \, \Delta \boldsymbol{d}^{s,n+1}_i = -\tilde{\mathcal{R}}^{dc}|^{n+1}_i, \tag{81}$$

which is an extension of (55) with a modified force residual vector $\tilde{\mathcal{R}}^{dc}$ emanating from the condensation of the discrete Lagrange multipliers and including contact forces (see $\mathcal{R}^{dc}$ in (67)). Similarly, the modified effective tangent matrix $\tilde{\boldsymbol{L}}_{dd}$ results from including contact stiffness terms, i.e. linearization of $\mathcal{R}^{dc}$, and again from performing condensation of the discrete Lagrange multipliers (see [21,22] for details). Another advantage of the presented contact formulation is the fact that neither a regularization (usually introduced via an unphysical and problem-specific penalty parameter) nor a costly augmentation scheme (usually based on an Uzawa-type algorithm) is necessary. The dual Lagrange multipliers allow for the contact constraints to be enforced exactly. Still, the method is very efficient due to the consistently linearized semi-smooth Newton approach for the active set search. All types of nonlinearities are resolved within one single iterative scheme. An extension to frictional sliding is possible without conceptual changes and has recently been presented for the 2D case [11].

5 Fluid–structure-(contact) coupling

In the previous two sections, we derived a linearized monolithic system of equations, which contains the fluid formulation, the structural formulation, the contact formulation as well as the coupling conditions at the fluid–structure interface in terms of an additional stress field $\boldsymbol{\sigma}$

$$\begin{bmatrix} \boldsymbol{L}_{uu} & \boldsymbol{L}_{up} & \boldsymbol{L}_{u\sigma} & \boldsymbol{0} \\ \boldsymbol{L}_{pu} & \boldsymbol{L}_{pp} & \boldsymbol{0} & \boldsymbol{0} \\ \boldsymbol{L}_{\sigma u} & \boldsymbol{L}_{\sigma p} & \boldsymbol{L}_{\sigma\sigma} & \boldsymbol{L}_{\sigma d} \\ \boldsymbol{0} & \boldsymbol{0} & \boldsymbol{L}_{d\sigma} & \tilde{\boldsymbol{L}}_{dd} \end{bmatrix} \begin{bmatrix} \Delta\boldsymbol{u} \\ \Delta\boldsymbol{p} \\ \Delta\boldsymbol{\sigma} \\ \Delta\boldsymbol{d}^s \end{bmatrix} = \begin{bmatrix} -\mathcal{R}^u \\ -\mathcal{R}^p \\ -\mathcal{R}^\sigma \\ -\tilde{\mathcal{R}}^{dc} \end{bmatrix}. \quad (82)$$

The unknown stress field $\boldsymbol{\sigma}$ can be condensed on the element level

$$\Delta\boldsymbol{\sigma} = \boldsymbol{L}_{\sigma\sigma}^{-1} \left(-\mathcal{R}^\sigma - \boldsymbol{L}_{\sigma u}\Delta\boldsymbol{u} - \boldsymbol{L}_{\sigma p}\Delta\boldsymbol{p} - \boldsymbol{L}_{\sigma d}\Delta\boldsymbol{d}^s \right). \quad (83)$$

By introducing the notation $\boldsymbol{L}_{u\sigma}^{\star} = \boldsymbol{L}_{u\sigma}\boldsymbol{L}_{\sigma\sigma}^{-1}$ and $\boldsymbol{L}_{d\sigma}^{\star} = \boldsymbol{L}_{d\sigma}\boldsymbol{L}_{\sigma\sigma}^{-1}$, the entries of the condensed linear system matrix result in

$$\boldsymbol{A}_{uu} = \boldsymbol{L}_{uu} - \boldsymbol{L}_{u\sigma}^{\star}\boldsymbol{L}_{\sigma u}, \quad (84)$$
$$\boldsymbol{A}_{up} = \boldsymbol{L}_{up} - \boldsymbol{L}_{u\sigma}^{\star}\boldsymbol{L}_{\sigma p}, \quad (85)$$
$$\boldsymbol{A}_{u\sigma} = -\boldsymbol{L}_{u\sigma}^{\star}\boldsymbol{L}_{\sigma d}, \quad (86)$$
$$\boldsymbol{A}_{pu} = \boldsymbol{L}_{pu}, \quad (87)$$
$$\boldsymbol{A}_{pp} = \boldsymbol{L}_{pp}, \quad (88)$$
$$\boldsymbol{A}_{du} = -\boldsymbol{L}_{d\sigma}^{\star}\boldsymbol{L}_{\sigma u}, \quad (89)$$
$$\boldsymbol{A}_{dp} = -\boldsymbol{L}_{d\sigma}^{\star}\boldsymbol{L}_{\sigma p}, \quad (90)$$
$$\boldsymbol{A}_{dd} = \tilde{\boldsymbol{L}}_{dd} - \boldsymbol{L}_{d\sigma}^{\star}\boldsymbol{L}_{\sigma d}. \quad (91)$$

The condensed coupled system

$$\begin{bmatrix} \boldsymbol{A}_{uu} & \boldsymbol{A}_{up} & \boldsymbol{A}_{ud} \\ \boldsymbol{A}_{pu} & \boldsymbol{A}_{pp} & \boldsymbol{0} \\ \boldsymbol{A}_{du} & \boldsymbol{A}_{dp} & \boldsymbol{A}_{dd} \end{bmatrix} \begin{bmatrix} \Delta\boldsymbol{u} \\ \Delta\boldsymbol{p} \\ \Delta\boldsymbol{d}^s \end{bmatrix} = \begin{bmatrix} -\mathcal{R}^u + \boldsymbol{L}_{u\sigma}^{\star}\mathcal{R}^\sigma \\ -\mathcal{R}^p \\ -\tilde{\mathcal{R}}^{dc} + \boldsymbol{L}_{d\sigma}^{\star}\mathcal{R}^\sigma \end{bmatrix} \quad (92)$$

may be solved by any state-of-the-art fluid–structure coupling scheme. The integrated dual mortar contact formulation does not restrict the application of coupling algorithms in any way. There exist mainly two classes of coupling algorithms: monolithic and partitioned schemes. In the case of monolithic schemes, the system may be solved directly e.g. by a truly monolithic algebraic multigrid solver tailored for fluid–structure interaction problems [6]. In the latter case, the monolithic system is partitioned and solved iteratively by different strong coupling schemes [15].

6 Numerical examples

We present one 2D and one 3D numerical example to illustrate the capabilities of our approach. All simulations are based on a parallel implementation of the algorithms described above in our research code BACI [33]. Since our implementation is 3D, the 2D example is modelled as a 3D problem with just one layer of elements in the third direction.

6.1 Contact of a 2D elastic structure with a stiff wall

In the first example, the capability of our proposed approach to deal with large structural deformations and contact is demonstrated. A hollow quadrangular structure ($E = 2000$, Poisson ratio $\nu = 0.4$) with rounded corners is positioned in a 2D channel flow, see Fig. 6. A parabolic inflow profile as Dirichlet boundary is applied at the top and a zero traction Neumann boundary is assumed at the bottom left and right. All remaining channel boundaries are stiff walls with contact occurring between the hollow structure and the bottom wall. 20-node hexahedral elements are used for the fluid mesh and 8-node hexahedral elements for the structural discretization. There is only one element layer in thickness direction and plane strain conditions are enforced by constraining any movement orthogonal to the paper-plane.

Flow field and structural deformation including contact are illustrated in Fig. 6, giving an impression of the highly dynamic fluid–structure-contact interaction (FSCI) process. Owing to its high flexibility the structure exhibits large deformations: At first, they are primarily induced by fluid stresses resulting from the increasing fluid pressure between the hollow structure and the bottom wall. At later stages the structural deformation is dominated by dry contact interaction. In Fig. 7, the contact forces acting in the contact zone are visualized for the stage of maximum structural deformation. Due to the very coarse structure mesh a small geometrical asymmetry is introduced, which explains why the contact forces are slightly asymmetric as well.

6.2 Contact of a 3D elastic torus with a stiff wall

The second test case illustrates a three-dimensional fluid–structure-contact interaction example. An elastic torus ($E = 4000$, Poisson ratio $\nu = 0.4$) turned around the y-axis by an angle of 65 degrees is placed in a 3D channel as depicted in Fig. 8. Similar to the settings in the example above, a parabolic inflow profile is imposed at the top boundary of the channel and zero traction Neumann boundaries allow outflow on the left and right side near the bottom. All other channel boundaries are no-slip boundaries. Both the fluid and the structural mesh consist of 8-node hexahedral elements. The velocity field around the moving torus is depicted in Fig. 8. Stream lines illustrate the 3D fluid flow through the inner hole of the torus before contacting with the wall. At first, the torus is moving towards the wall due to the interaction with the fluid stresses. The exact interface representation allows to resolve flow patterns around the torus very close to contact and to simulate dry contact. After some time, the torus touches the wall and its further movement and deformation is influenced by the fluid at the fluid–structure interface and by contact forces at the contact interface.

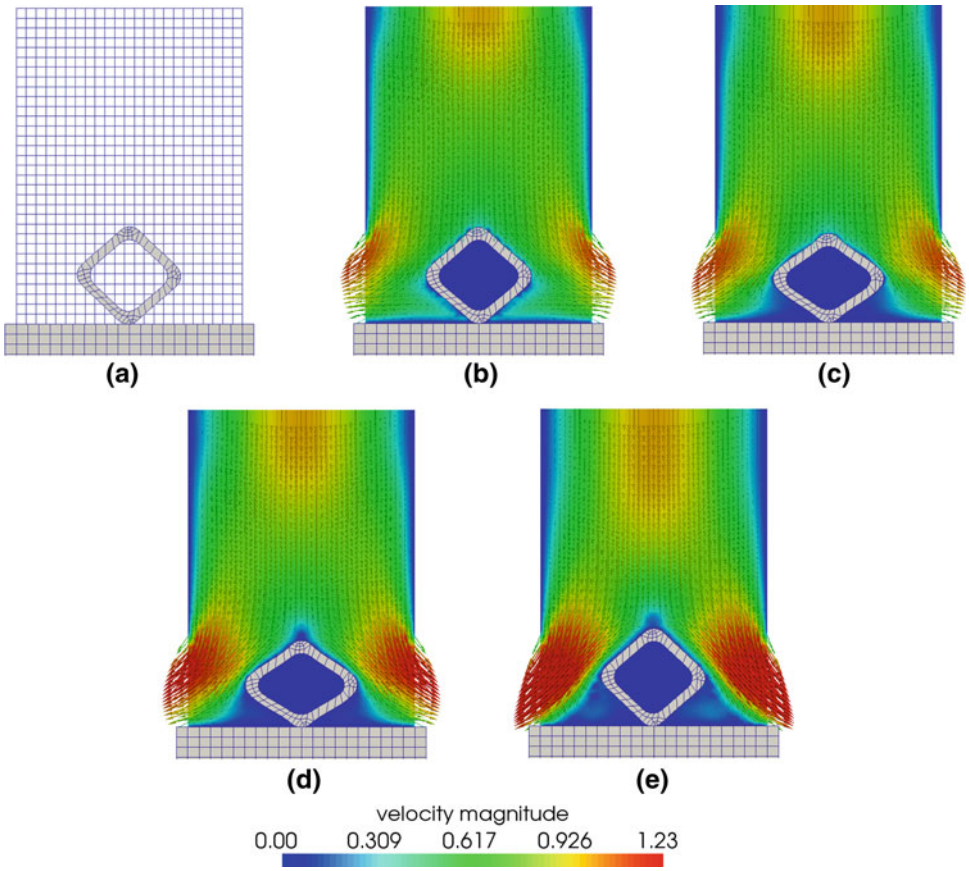

Fig. 6 Flexible structure contacting a stiff wall: **a** finite element mesh, **b–e** fluid velocity and structural deformation are visualized for several time steps of the dynamic fluid–structure-contact interaction process

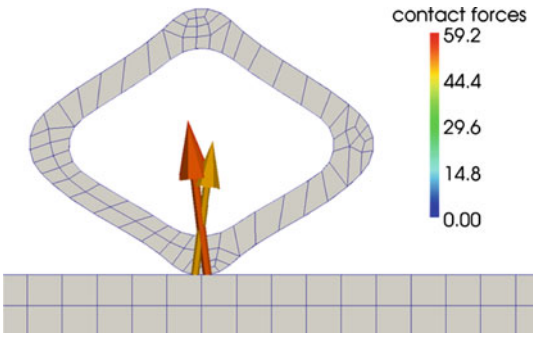

Fig. 7 2D structure contacting a stiff wall—contact forces

7 Conclusions

We propose a three-dimensional finite element approach to finite deformation contact of structures embedded in fluid flows. The possibility to simulate finite deformation contact of solids in fluid flows allows to investigate a wide range of engineering problems, which so far could hardly be solved. The presented fluid–structure-contact interaction (FSCI) method combines algorithmically a dual mortar contact formulation with an XFEM FSI method. The FSI approach as well as its combination with the contact formulation does not introduce any restrictions to the structural formulation. The resulting linearized coupled system comprising the fluid formulation, the structural formulation as well as the contact formulation may be solved by either partitioned or monolithic state-of-the-art fluid–structure coupling schemes. An exact interface representation allows for highly accurate flow computations around the interface of structures in contact and for the simulation of dry contact.

One possibility to extend the approach is to include wet contact e.g. based on a lubrication model as an intermediate layer between dry contact and a full FSI computation. Current work also considers the integration of the reviewed macroscopic contact formulation within a mesoscopic FSI approach [18] for biophysical problems. On the mesoscopic scale, structures are interacting through intermolecular interaction phenomena. Under certain circumstances, intermolecular interaction of structures very close to contact can be extended or approximated by a macroscopic contact formulation.

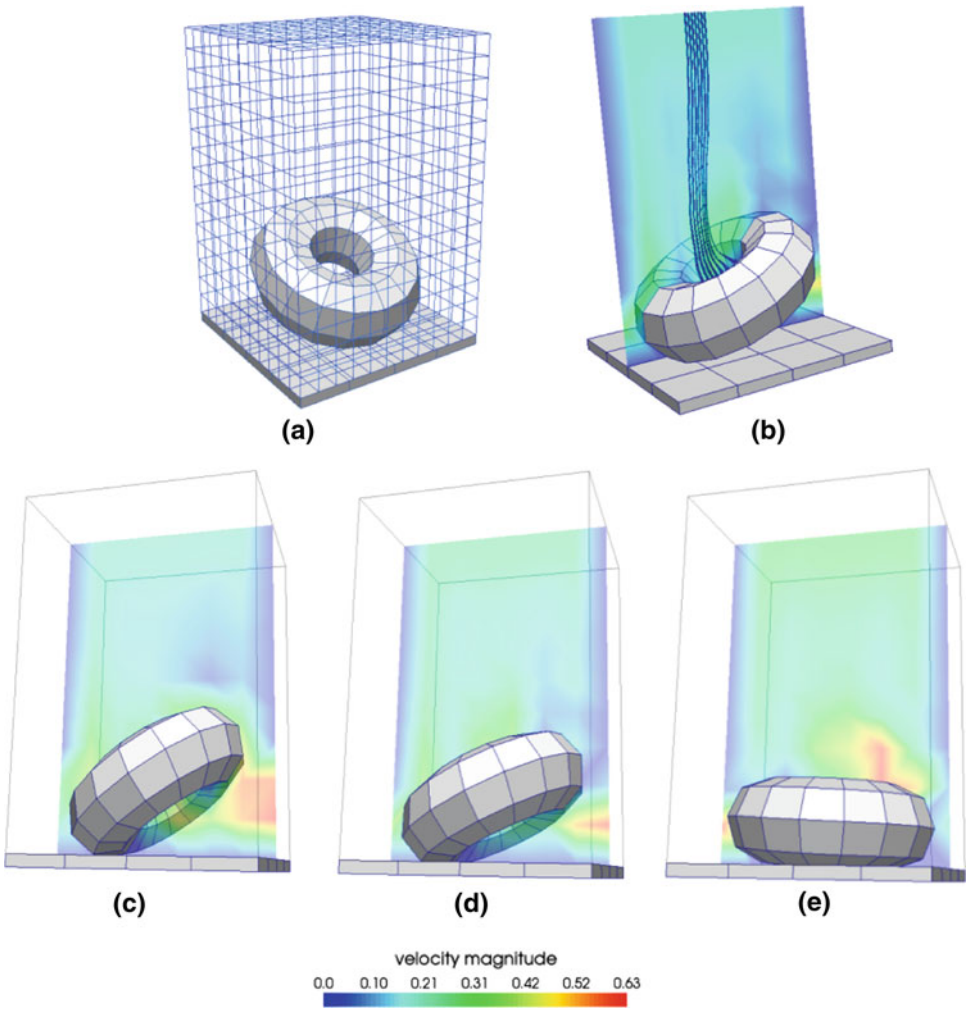

Fig. 8 3D torus contacting a stiff wall: **a** finite element mesh, **b** stream lines through the inner hole of the torus before contact, **c**–**e** fluid velocity and structural movement are visualized for several time steps of the dynamic fluid–structure-contact interaction process

Acknowledgments The support of the first author by the International Graduate School for Science and Engineering (IGSSE) of Technische Universität München is gratefully acknowledged.

References

1. Astorino M, Gerbeau J-F, Pantz O, Traor K-F (2009) Fluid–structure interaction and multi-body contact: application to aortic valves. Comput Methods Appl Mech Eng 198(45–46):3603–3612
2. Belytschko T, Black T (1999) Elastic crack growth in finite elements with minimal remeshing. Int J Numer Methods Eng 45(5):601–620
3. Chung J, Hulbert GM (1993) A time integration algorithm for structural dynamics with improved numerical dissipation: the generalized-alpha method. J Appl Mech 60:371–375
4. Diniz dos Santos N, Gerbeau J-F, Bourgat J-F (2008) A partitioned fluid–structure algorithm for elastic thin valves with contact. Comput Methods Appl Mech Eng 197(19–20):1750–1761
5. Förster Ch, Wall WA, Ramm E (1999) On the geometric conservation law in transient flow calculations on deforming domains. Int J Numer Methods Fluids 50:1369–1379
6. Gee MW, Küttler U, Wall WA (2009) Truly monolithic algebraic multigrid for fluid–structure interaction. Int J Numer Methods Eng (submitted)
7. Gerstenberger A, Wall WA (2008) Enhancement of fixed-grid methods towards complex fluid–structure interaction applications. Int J Numer Methods Fluids 57(9):1227–1248
8. Gerstenberger A, Wall WA (2008) An extended finite element method/Lagrange multiplier based approach for fluid–structure interaction. Comput Methods Appl Mech Eng 197:1699–1714
9. Gerstenberger A, Wall WA (2009) An embedded dirichlet formulation for 3d continua. Int J Numer Methods Eng (accepted)
10. Gerstenberger A, Wall WA (2010) A fixed-grid approach to three-dimensional fluid–structure interaction (in preparation)
11. Gitterle M, Popp A, Gee MW, Wall WA (2010) Finite deformation frictional mortar contact using a semi-smooth Newton method with consistent linearization. Int J Numer Methods Eng (accepted)
12. Hartmann S, Brunssen S, Ramm E, Wohlmuth B (2007) Unilateral non-linear dynamic contact of thin-walled structures using a primal-dual active set strategy. Int J Numer Methods Eng 70(8):883–912
13. Hintermüller M, Ito K, Kunisch K (2002) The primal-dual active set strategy as a semismooth Newton method. SIAM J Optim 13(3):865–888

14. Hüeber S, Wohlmuth B (2005) A primal-dual active set strategy for non-linear multibody contact problems. Comput Methods Appl Mech Eng 194(27–29):3147–3166
15. Küttler U, Gee MW, Förster Ch, Comerford A, Wall WA (2009) Coupling strategies for biomedical fluid–structure interaction problems. Int J Numer Methods Biomed Eng (accepted)
16. Laursen TA (2002) Computational contact and impact mechanics. Springer, Berlin
17. Mayer UM, Gerstenberger A, Wall WA (2009) Interface handling for three-dimensional higher-order XFEM computations in fluid–structure interaction. Int J Numer Methods Eng 79:846–869
18. Mayer UM, Wall WA (2010) A finite element approach to 3D intermolecular & surface interaction of multiple flexible mesoscopic structures in fluid flow (in preparation)
19. Mayer UM, Wall WA (2010) Efficient parallel search algorithms in (mesoscopic) fluid–structure interaction (in preparation)
20. Moes N, Dolbow J, Belytschko T (1999) A finite element method for crack growth without remeshing. Int J Numer Methods Eng 46:131–150
21. Popp A, Gee MW, Wall WA (2009) A finite deformation mortar contact formulation using a primal-dual active set strategy. Int J Numer Methods Eng 79:1354–1391
22. Popp A, Gitterle M, Gee MW, Wall WA (2010) A dual mortar approach for 3d finite deformation contact with consistent linearization. Int J Numer Methods Eng (accepted)
23. Puso MA (2004) A 3D mortar method for solid mechanics. Int J Numer Methods Eng 59(3):315–336
24. Puso MA, Laursen TA (2004) A mortar segment-to-segment contact method for large deformation solid mechanics. Comput Methods Appl Mech Eng 193(6–8):601–629
25. Puso MA, Laursen TA (2004) A mortar segment-to-segment frictional contact method for large deformations. Comput Methods Appl Mech Eng 193(45–47):4891–4913
26. Qi L, Sun J (1993) A nonsmooth version of Newton's method. Math Program 58(1):353–367
27. Sathe S, Tezduyar TE (2008) Modeling of fluid–structure interactions with the space–time finite elements: contact problems. Comput Mech 43(1):51–60
28. Tezduyar TE, Behr M, Liou J (1992) A new strategy for finite element computations involving moving boundaries and interfaces—the deforming-spatial-domain/space–time procedure. I. The concept and the prelimianry numerical tests. Comput Methods Appl Mech Eng 94:339–351
29. Tezduyar TE, Behr M, Mittal S, Liou J (1992) A new strategy for finite element computations involving moving boundaries and interfaces – the deforming-spatial-domain/space-time procedure. II. Computation of free-surface flows, two-liquid flows, and flows with drifting cylinders. Comput Methods Appl Mech Eng 94: 353–371
30. Tezduyar TE, Sathe S (2007) Modelling of fluid–structure interactions with the space-time finite elements: solution techniques. Int J Numer Methods Fluids 54(6-8):855–900
31. van Loon R, Anderson PD, van de Vosse FN (2006) A fluid–structure interaction method with solid-rigid contact for heart valve dynamics. J Comput Phys 217(2):806–823
32. Wall WA, Gamnitzer P, Gerstenberger A (2008) Fluid–structure interaction approaches on fixed grids based on two different domain decomposition ideas. Int J Comput Fluid Dyn 22(6):411–427
33. Wall WA, Gee MW (2009) Baci—a multiphysics simulation environment. Technical report, Technische Universität München
34. Wall WA, Gerstenberger A, Mayer UM (2008) Advances in fixed-grid fluid structure interaction. In: ECCOMAS multidisciplinary jubilee symposium—new computational challenges in materials, structure and fluids 14:235–249
35. Wohlmuth BI (2000) A mortar finite element method using dual spaces for the Lagrange multiplier. SIAM J Numer Anal 38(3):989–1012
36. Wohlmuth BI (2001) Discretization methods and iterative solvers based on domain decomposition. Springer, Berlin
37. Wriggers P (2002) Computational contact mechanics. John Wiley & Sons, New York
38. Yang B, Laursen TA (2009) A mortar-finite element approach to lubricated contact problems. Comput Methods Appl Mech Eng 198:3656–3669
39. Yang B, Laursen TA, Meng X (2005) Two dimensional mortar contact methods for large deformation frictional sliding. Int J Numer Methods Eng 62(9):1183–1225